

NASA Contractor Report 191589

ICASE Report No. 93-101

ICASE



**VORTEX GENERATION AND WAVE-VORTEX INTERACTION
OVER A CONCAVE PLATE WITH ROUGHNESS AND SUCTION**

Fabio Bertolotti

NASA Contract No. NAS1-19480
December 1993

Institute for Computer Applications in Science and Engineering
NASA Langley Research Center
Hampton, Virginia 23681-0001

Operated by the Universities Space Research Association



National Aeronautics and
Space Administration

Langley Research Center
Hampton, Virginia 23681-0001

VORTEX GENERATION AND WAVE-VORTEX INTERACTION OVER A CONCAVE PLATE WITH ROUGHNESS AND SUCTION

Fabio P. Bertolotti ¹

DLR, Institut für Theoretische Strömungsmechanik
Bunsenstr. 10, D-37073 Göttingen, Germany

ABSTRACT

The generation and amplification of vortices by surface inhomogeneities, both in the form of surface waviness and of wall-normal velocity, is investigated using the nonlinear PSE equations. Transients and issues of algebraic growth are avoided through the use of a similarity solution as initial condition for the vortex.

In the absence of curvature, the vortex decays as $\sqrt{1/x}$ when flowing over streamwise aligned riblets of constant height, and grows as \sqrt{x} when flowing over a corresponding streamwise aligned variation of blowing/suction transpiration velocity. However, in the presence of wall inhomogeneities having both streamwise and spanwise periodicity, the growth of the vortex can be much larger. In the presence of curvature, the vortex develops into a Görtler vortex.

The “direct” and “indirect” interaction mechanisms possible in wave-vortex interaction are presented. The “direct” interaction does not lead to strong resonance with the flow conditions investigated. The “indirect” interaction leads to K-type transition.

¹This research was supported by the National Aeronautics and Space Administration under NASA Contract No. NAS1-19480 while the author was in residence at the Institute for Computer Applications in Science and Engineering (ICASE), NASA Langley Research Center, Hampton, VA 23681.

1 Introduction

We present results from an investigation into the laminar-turbulent transition process over a plate with wall undulations, wall blowing & suction, and concave curvature. The investigation is based on numerical simulations using the nonlinear PSE equations. The curvature is sufficiently small to allow the Blasius profile to be used as the mean-flow in all the conditions investigated. The particular topics covered in this report are:

1. The seeding of Görtler vortices by streamwise aligned wall corrugations and blowing/suction inhomogeneities.
2. The receptivity of vortices to three dimensional wall corrugations and blowing/suction inhomogeneities.
3. The effect of curvature on three-dimensional TS waves.
4. Some cases of nonlinear wave-vortex interactions.

Two geometries are considered. Figure 1a displays the geometry used in the study of topic 1. The wall corrugations vary sinusoidally in the spanwise direction, z , with a wavenumber β , and have the crests aligned in the streamwise, or x , direction. The label x_k denotes the location at which the curvature departs from zero and increases downstream up to a constant final value. The initial location for the PSE marching solution, x_0 , is upstream of x_k .

Figure 1b displays the geometry used in the study of the receptivity of vortices (Görtler and other types) to wall corrugations which vary sinusoidally in both x and z (topic 2). This receptivity problem is steady in time. Moreover, when the acoustic source is added (represented in the figure by the speaker), the distributed receptivity mechanism described by Crouch [1] is activated, creating Tollmien-Schlichting waves. These waves then interact with the vortex (topic 4).

In figure 1, the wall undulation can be interpreted as either a physical undulation present on the plate surface, or, in the case of blowing/suction, as an iso-level of wall-normal velocity on a smooth plate. The height of the wall undulation is of the order of 0.1% of the boundary layer thickness, hence the undulation can represent imperfections on wing surfaces due to, for example, temperature or direct stresses in flight. The peak surface transpiration velocity in the blowing and suction study is of order of $1 \times 10^{-4} U_\infty$, in agreement with levels used in Laminar Flow Control experiments (P. Spalart, personal communication).

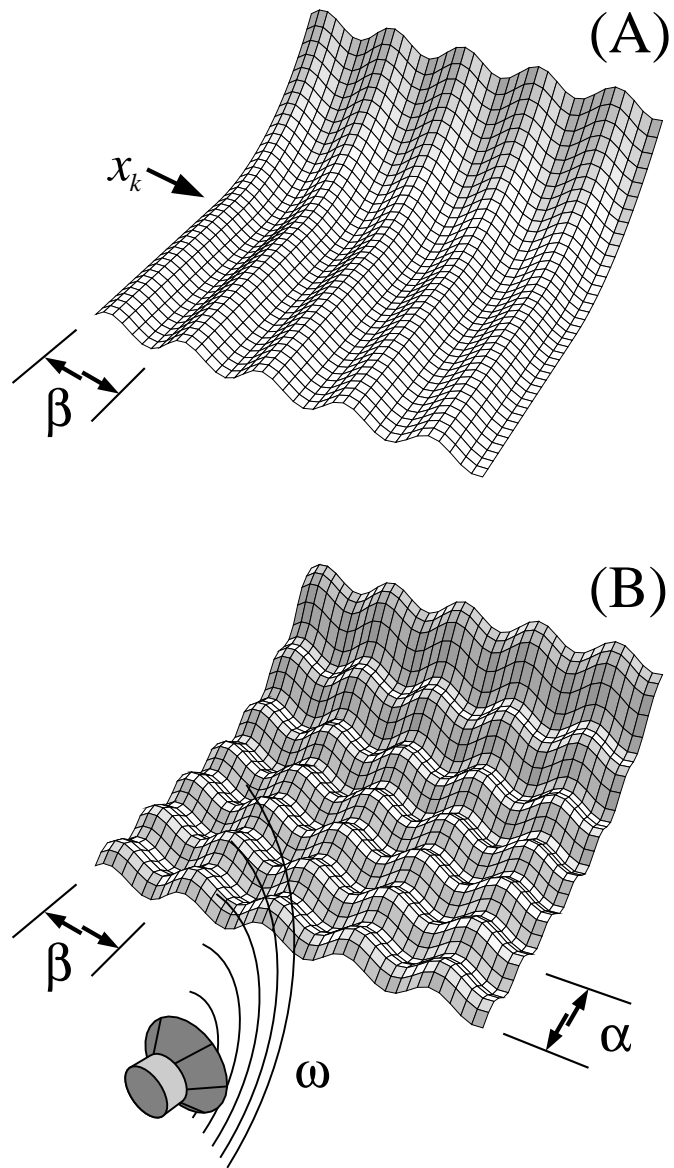


Figure 1: Geometry used in the simulation. Top, the corrugated plate with an initial flat section, followed by a section of concave curvature. Bottom, the same geometry as above with wall undulations in the streamwise direction added, as well as acoustic forcing.

The main results corresponding to the topics listed above are:

1. Wall-aligned corrugations provide an efficient means for the generation of Görtler vortices.
2. Vortices exhibit growth when flowing over three dimensional wall corrugations or blowing/suction inhomogeneities, even in the absence of curvature. This receptivity persists when the wavenumbers of the wall inhomogeneities differ greatly from those of the vortex, i.e. short wavelength undulations in x and z can force a large wavelength vortex.
3. The neutral stability curves for three-dimensional TS waves enlarge in size as curvature is increased, and eventually extend to zero frequency; thus connecting with the Görtler vortices.
4. The direct and indirect wave-vortex interaction is presented. The indirect interaction leads to a K-type resonant triad, while the direct interaction shows no wave-vortex resonance at the conditions investigated.

A brief description of the PSE equations and the numerical algorithm employed to solve them is given in the appendix A. We also describe, in appendix B, the construction of a self-similar solution that, when used as initial condition for the vortex in the PSE marching procedure, yields results free of transients and of algebraic growth (see Schimd and Henningson [2]). The self-similar solution, thus, allows for the investigation of vortex receptivity to distributed forcing. Otherwise, if an initial condition is used that leads to strong algebraic growth, the effects of the distributed forcing will be masked. A similarity solution for the Görtler vortex was first presented by Denier, Hall & Seddougui [3] in their investigation of vortex forcing from a plate with a localized hump.

1.1 Reference quantities, and geometry description

The reference length chosen is $\delta_r^* = \sqrt{\nu^* x_{1000}^* / U_\infty^*}$ where x_{1000}^* is the location at which the Reynolds number $R_x = U_\infty x_{1000}^* / \nu^*$ equals 1×10^6 . The symbol * denotes a dimensional quantity. This reference length is used throughout this report, with the exception of appendix B, which deals with the self-similar solution.

The non-dimensional curvature is $\mathcal{K} = \delta_r^* / a_{kur}^*$, where a_{kur}^* is the radius of curvature. Typical values of \mathcal{K} are 1, 2, 4 and 8×10^{-4} . In the case of a subsonic wind-tunnel test with $U_\infty = 15$ m/s, the reference length is $\delta_r^* = 1.2$ mm, and the radius of curvature is 12, 6, 3 and 1.5 meters respectively.

The coordinate along the streamwise direction is x , the plate normal direction is y , and the spanwise direction is z . The corresponding velocity components are u , v , and w . The representation of the flow-field is described in appendix A.

All modes are identified with the three integers in the triplet $\mathbf{p} = (l, n, k)$, corresponding to the indices in the Fourier expansion $e^{in\alpha x + ik\beta z - i\omega t}$. The values of α , β and ω are prescribed as input parameters to the PSE calculation. The wavy-wall surface is represented by the function,

$$H(x, z) = \sum_{n=-N}^N \sum_{k=-K}^K \mathcal{W}_{(0,n,k)} e^{in\alpha x + ik\beta z} + \text{c.c} \quad (1)$$

where “c.c” denotes complex conjugate. The coefficients \mathcal{W} are complex constants. The boundary conditions over the wavy wall are transferred to $y = 0$ via a Taylor series expansion (see appendix A). The blowing/suction wall normal velocity is described by,

$$V_{suc}(x, z) = \sum_{n=-N}^N \sum_{k=-K}^K \mathcal{S}_{(0,n,k)} e^{in\alpha x + ik\beta z} + \text{c.c} \quad (2)$$

The boundary conditions at the wall satisfied by the disturbances are then,

$$u_{\mathbf{p}} = 0 \quad v_{\mathbf{p}} = \mathcal{S}_{(0,n,k)} \quad w_{\mathbf{p}} = 0 \quad (3)$$

The homogeneous boundary condition for $u_{\mathbf{p}}$ and $w_{\mathbf{p}}$ implies weak suction rates (Spalart [4]). Lastly, in the presentation of the results we use the local Reynolds number $R = \sqrt{\nu^* x^* / U_{\infty}^*} = \sqrt{R_x}$, and the nondimensional frequency $F = 2\pi f^* U_{\infty}^{*2} / \nu^*$, where f^* is the dimensional frequency in Hz.

2 Validation of the self-similar vortex

The construction of the self-similar vortex solution is described in appendix B. Here, we present the results which prove that the assumptions and approximations used to obtain the self-similar formulation are sound.

A test for the accuracy of the self-similar form of the vortex field can be made by running the PSE using as initial conditions the solution to (19) and (20). If the PSE solution remains close to self-similar over a downstream range sufficiently long to otherwise display algebraic growth and decay, then the self-similar approximation provides an acceptable initial condition for vortices in both direct numerical simulations of the Navier-Stokes equations, and in PSE integrations. The test was run using the linearized PSE equations with the initial condition given at $R = 300$. The riblets on the wall were held constant at an amplitude of $0.004 \delta_{(R=300)}^*$, while in the suction case, the level was held constant at 1×10^{-5} . Figure 2 displays the maximum amplitude of the u velocity component as function of Reynolds number, for various values of the spanwise wavenumber $\beta^1 = \beta^* \delta_{(R=300)}^*$. Note the absence of transients in the plot. In the case of the wall riblet, the amplitude decreases with streamwise distance due to the following reason: the maximum of the u velocity occurs at $y = 0$ where the boundary condition (21) imposes a constant amplitude for u_{self} , and the physical u is related to the self-similar u_{self} by the factor x_0/x . On the other hand, constant suction leads to a self-similar vortex with u_{max} increasing proportional to \sqrt{x} . The departure of the PSE solution from the self-similar one as β is increased shows the error introduced by freezing the coefficient $\beta^2(x/x_0)$ in the self-similar formulation.

Figure 3 displays the velocities $u_{self}(\eta)$ and $v_{self}(\eta)$ at the initial location $R = 300$, and downstream, at $R = 1136$ and 1670 . The dots trace the shape of the self-similar functions $u_{self}(\eta)$ and $v_{self}(\eta)$, while the solid and dashed lines show the corresponding profiles obtained by extracting the u_{self} and v_{self} profiles from those given by the PSE equations at $R = 300$ to $R = 980$ and $R = 1600$. Both the u and the v velocity components computed with the PSE collapse close to the self-similar profiles. This agreement, along with the absence of algebraic growth or other transients, validates the assumptions and approximations used in generating the self-similar solution.

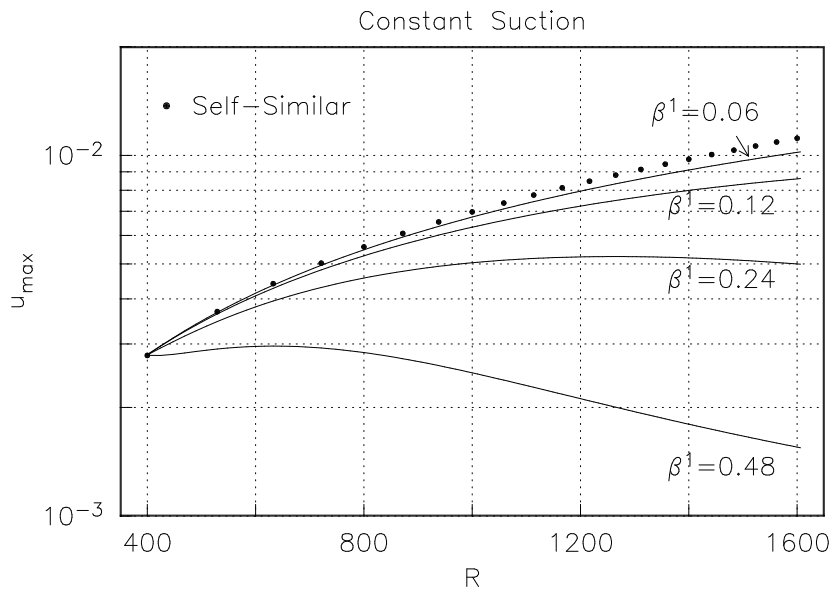
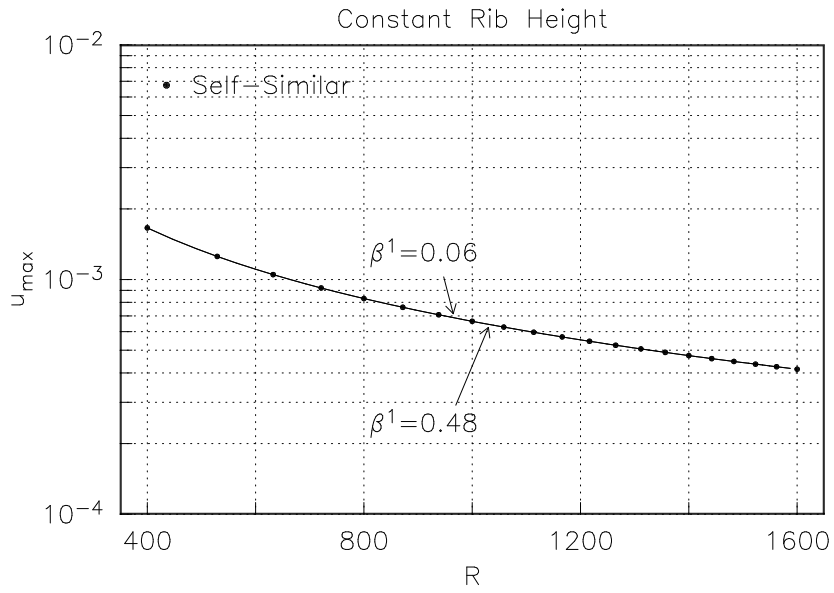
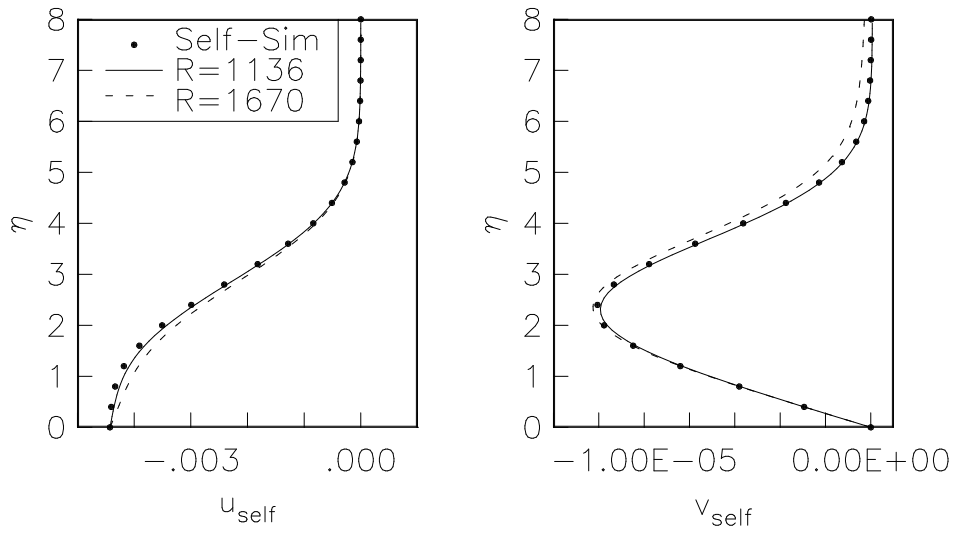


Figure 2: Self-Similar amplitudes

Constant Rib



Constant Suction

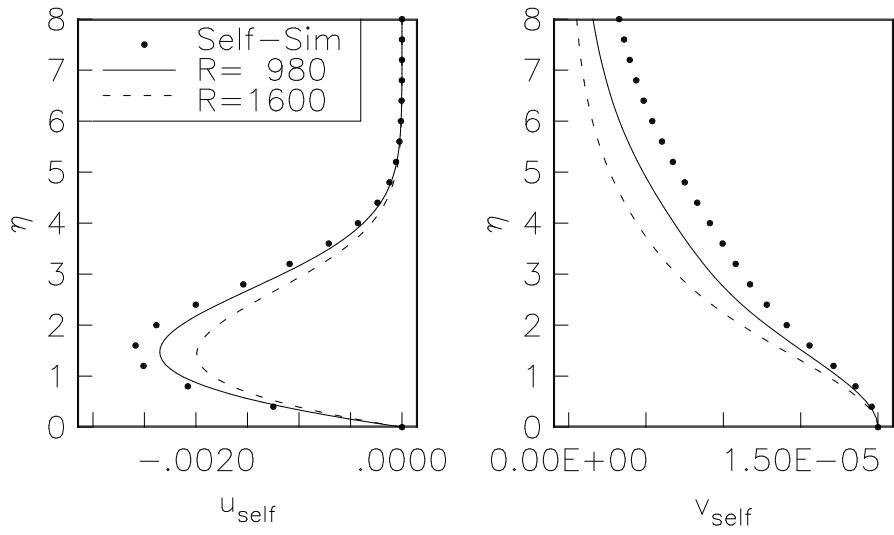


Figure 3: Self-Similar profiles

3 Vortex Seeding

The generation of Görtler vortices by a localized hump was investigated by Denier, Hall & Seddougui [3], and found that the mechanism was inefficient in generating vortices. Later, Bassom and Hall [5] corrected some errors and extended the work, and found that distributed forcing functions are much more efficient in the generation of Görtler vortices.

We study the birth and growth of the Görtler vortices that develop on top of the corrugated (i.e. ribbed) plate with a concave curvature. Initially, the curvature of the corrugated plate is zero, and is increased smoothly from zero at $R = 300$ to the maximum constant value at $R \geq 500$ with a half-period cosine function.

At the onset of curvature, the flow is composed of the Blasius flow plus the self similar solution discussed above. Downstream, Görtler vortices develop with the same spanwise wavenumber as the wall corrugation. The self-similar solution has a non-zero projection onto the Görtler eigenmode, and, thus, provides the initial amplitude for the vortex.

The five cases studied are categorized by the variation in x of the wall corrugations. The case ‘infinite’ has constant amplitude for all $R \geq 300$; the case ‘400-500’ has a constant amplitude up to $R = 400$, then decreases smoothly to zero between $400 < R < 500$ and remains zero afterwards; the cases ‘400-600’ and ‘400-800’ and ‘300-400’ are of equal nomenclature. For each case, 5 runs are made with the curvature taking on values of $\mathcal{K} = 0, 1 \times 10^{-4}, 2 \times 10^{-4}, 4 \times 10^{-4}$ and 8×10^{-4} . The spanwise wavenumber in all cases is $\beta = 0.15$. The calculation is maintained purely linear by artificially neglecting the nonlinear terms that arise from a finite amplitude vortex.

Figure 4 displays the maximum amplitude of the u component of velocity as function of Reynolds number. The plots on the left column of figure 4 display the u_{max} amplitude of the vortex mode versus Reynolds number for the cases ‘infinite’, ‘400-600’, and ‘300-400’. The Görtler vortex amplitude is plotted on the right column. This amplitude is computed by subtracting from the flow-field the flow field due to the wall corrugation in the absence of curvature.

The ‘infinite’ case produces the fastest growth of the Görtler mode. This fact suggests that the vortex is receptive to the forcing from the wall corrugation over an extended streamwise extent. Indeed, the extend seems larger than the region of strong nonlocal receptivity (Crouch[1], Crouch & Bertolotti [6]) for traveling waves. The growth rates in all cases asymptote to a single curvature-dependent value at $R = 1400$: the difference in amplitude at this position from case to case is due to the different corrugation geometry.

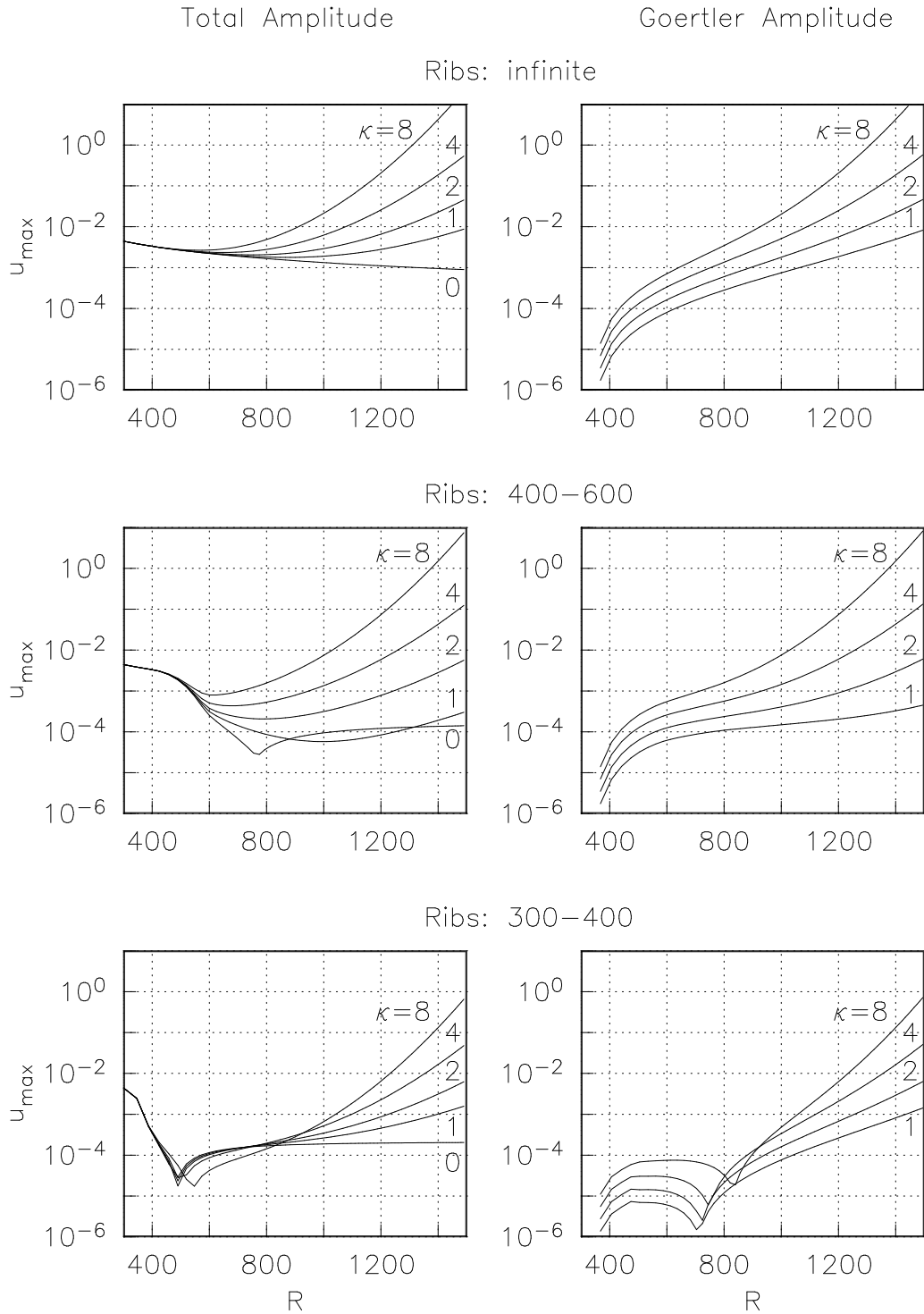


Figure 4: u_{max} amplitudes for various values of curvature, κ . The left column is the amplitude of the total disturbance, the right column is the amplitude of the Görtler vortex.

The ‘kink’ in the amplitude curves of the ‘400-600’ and ‘300-400’ cases occurs at the streamwise location where the decaying wall-mode’s u_{max} amplitude, which is maximum at the wall, equals the growing Görtler amplitude, which has a maximum at about $y = 2.5$.

An interesting phenomena can be seen in the amplitude plots of the Görtler vortex in the ‘300-400’ case. The kink in the amplitude curve in the neighborhood of $R = 800$ divides the upstream region dominated by the wall mode from the downstream region dominated by the Görtler vortex. The streamwise position of this kink shifts *downstream* when curvature is increased. This suggest that the wall-mode retards the growth of the Görtler vortex.

4 Vortex Receptivity

We study the effect of surface roughness on the growth of vortices. I have used the word “seeding” in the previous section and the word “receptivity” in this section to differentiate between the types of forcing given to the vortex. Seeding occurs when the forcing comes directly from the boundary condition, and hence, is a linear process (the word “seeding” was suggested by M. Morkovin in a private communication). Receptivity occurs when the forcing comes from the nonlinear interaction between other modes. In the absence of nonlinearity (or in the limit of small amplitude), these modes do not affect the vortex at all. In our case these modes are due to wall undulations or wall suction having wavenumbers different from that of the vortex.

In order to isolate the receptivity effect from centrifugal instabilities, we consider the case of a flat plate at zero angle of attack. The plate’s surface contains a spanwise periodic rib with streamwise aligned peaks and valleys. This rib generates the vortex - and at the initial marching location the vortex form is given by the self-similar solution. The height of the rib is constant in x , and corresponds to the coefficient $\mathcal{W}_{(0,0,2)} = 1 \times 10^{-3}$ (see equation 1). In addition to this rib, we add the source for other steady disturbances, either in the way of additional surface undulations, or using blowing and suction periodic in x and z . The height or strength of this additional source is increased from 0 to its final value using a ramp function starting at $R = 425$ and ending at $R = 700$. The gradual introduction of these modes reduces the amount of algebraic growth that is introduced into the evolution of the vortex.

The first set of results are for the case in which the wall contains one additional Fourier mode mode (besides the rib), having a streamwise wavenumber α that is varied parametrically, and a spanwise wavenumber β that is half that of the vortex. The indices for the wall mode are of the form $(0, n, 1)$, while that of

the vortex is $(0, 0, 2)$. Thus, the interaction of mode $(0, n, 1)$ with its companion mode $(0, -n, 1)$ (i.e. from symmetry in z) creates a forcing at $(0, 0, 2)$.

Figure 5 displays the results for the case of a wavy wall with Fourier coefficient $\mathcal{W}_{(0,n,1)} = 2 \times 10^{-3}$, and the case of blowing/suction with a coefficient $\mathcal{S}_{(0,n,1)} = 5 \times 10^{-5}$, for different values of α . In the wavy-wall case, increasing α increases the forcing efficiency. For $\alpha = 1.0$ the vortex increases one order in magnitude. In the suction case, the opposite trend exists; reducing α increases the forcing. The explanation for this opposite trends can be seen in the velocity profiles of the steady modes, shown in figure 6. Shortening the wavelength of the wavy-wall mode increases the slope $\partial u / \partial y$ at the wall, which is multiplied by the wall undulation height to produce the forcing (see equation (11)). On the other hand decreasing α , while holding the suction level constant, increases the u component of the velocity, hence the forcing in the interior of the domain.

The second set of results we present contain a pair of steady modes having a *difference* in spanwise wavenumber equal to the vortex's wavenumber,

$$\begin{aligned} \mathcal{W}_{(0,n,m)} &= 2 \times 10^{-3} & \mathcal{W}_{(0,n,m+2)} &= i 2 \times 10^{-3} \\ \mathcal{S}_{(0,n,m)} &= 5 \times 10^{-5} & \mathcal{S}_{(0,n,m+2)} &= i 5 \times 10^{-5} \end{aligned}$$

The quadratic nonlinearity then produces a forcing at $(0, 0, 2)$ for any value of n and m . In this way, short wavelength disturbances can directly influence long wave-length disturbances. This type of coupling was used by Crouch [7] in a study of TS wave receptivity to short-scale waviness. The phase-shift of 90 degrees between the two steady modes leads to a more effective forcing than the case were both Fourier coefficients \mathcal{W} are purely real.

Figure 7 displays the result for the combinations $n = 1, m = 2$, and $n = 1, m = 6$, with $\alpha = 1.0$ and $\beta = 0.15$. The vortex has a spanwise wavenumber of $\beta = 0.30$, as in the previous case. For reference, the case $\beta + \beta$ from figure 5 is included in the plot. The large vortex amplitude created by the “difference interactions” shows that the coupling between short and long wavelengths can be strong.

Figure 8a show the effect of the surface's undulation height on the evolution of the vortex. A height as small as 2.5×10^{-3} can produce a noticeable increase in vortex amplitude. For reference, it is useful to consider dimensional quantities. In a slow-speed wind-tunnel with a free-stream velocity of 10 m/s, the reference length is $\delta_o = 1.5$ mm (i.e. at $R = 1000$), thus the surface undulations are roughly 15 micrometers. This small value suggest that the distributed forcing from small plate undulations can introduce vortices in cases where the curvature is nominally zero. In particular, distributed forcing can be a cause

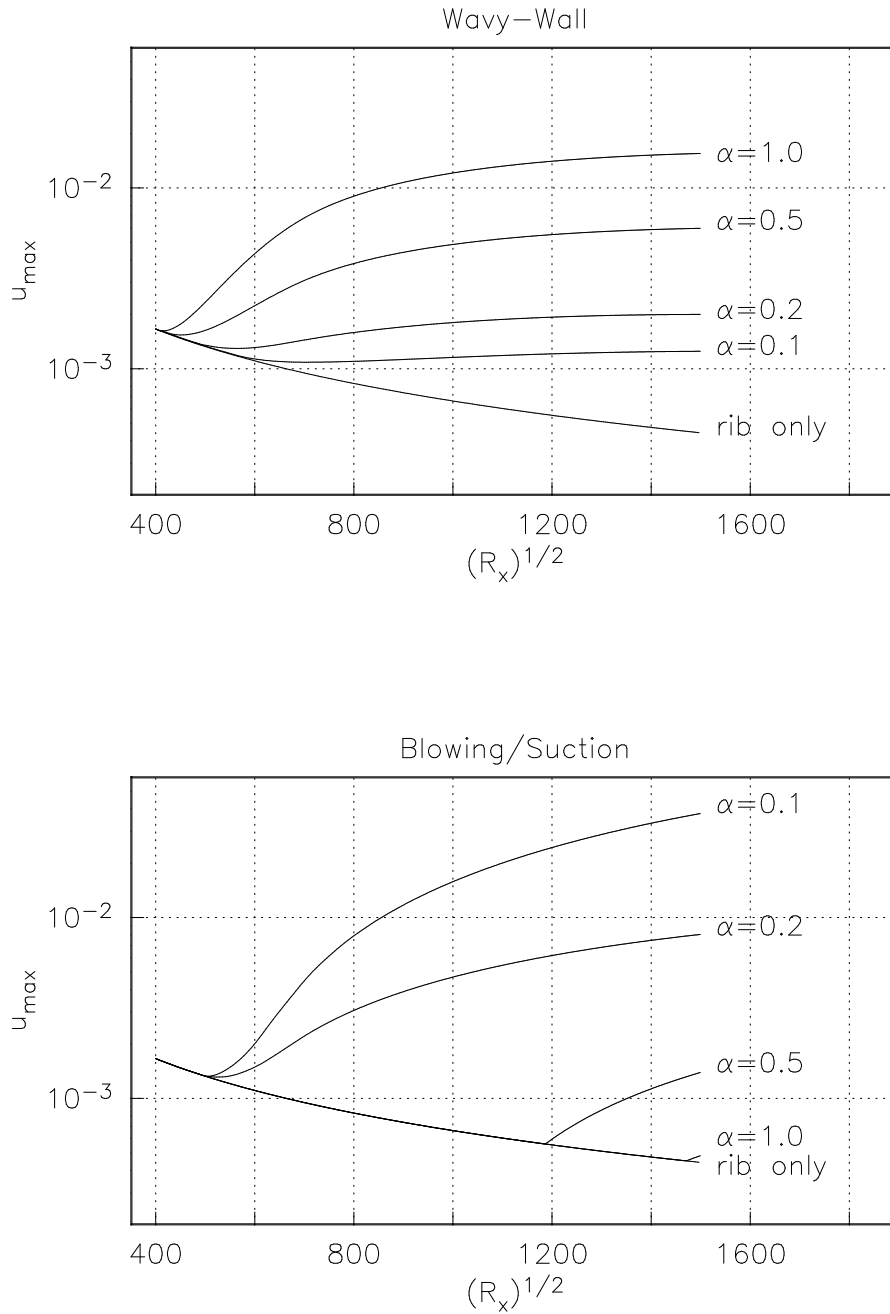


Figure 5: u_{max} amplitude versus Reynolds number of a vortex with spanwise wavenumber 2β flowing over a surface with wavenumber $(0, \alpha, \beta)$. Top, surface mode corresponds to surface undulation; bottom, surface mode corresponds to blowing/suction. The line labeled “rib only” shows the amplitude of the vortex flowing over the streamwise ribs only.

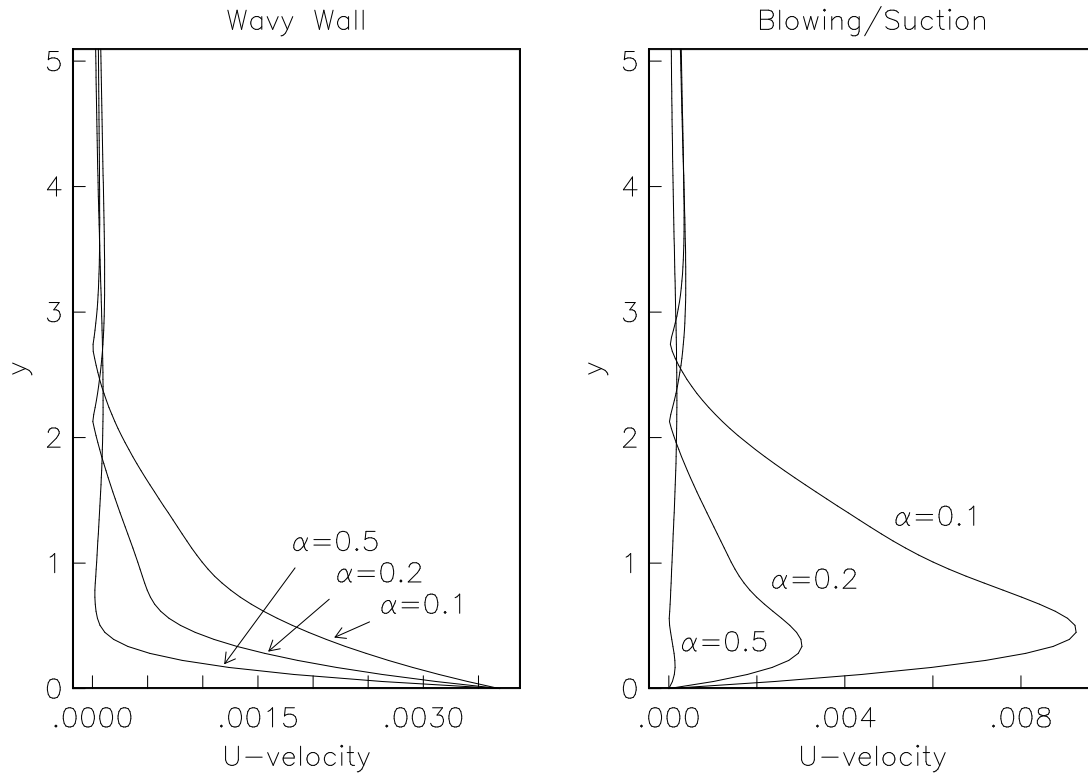


Figure 6: u velocity profiles at $R = 600$ due to a wavy-wall, left, and suction, right, with spanwise wavenumber $\beta = 0.3$ and different values of streamwise wavenumber α .

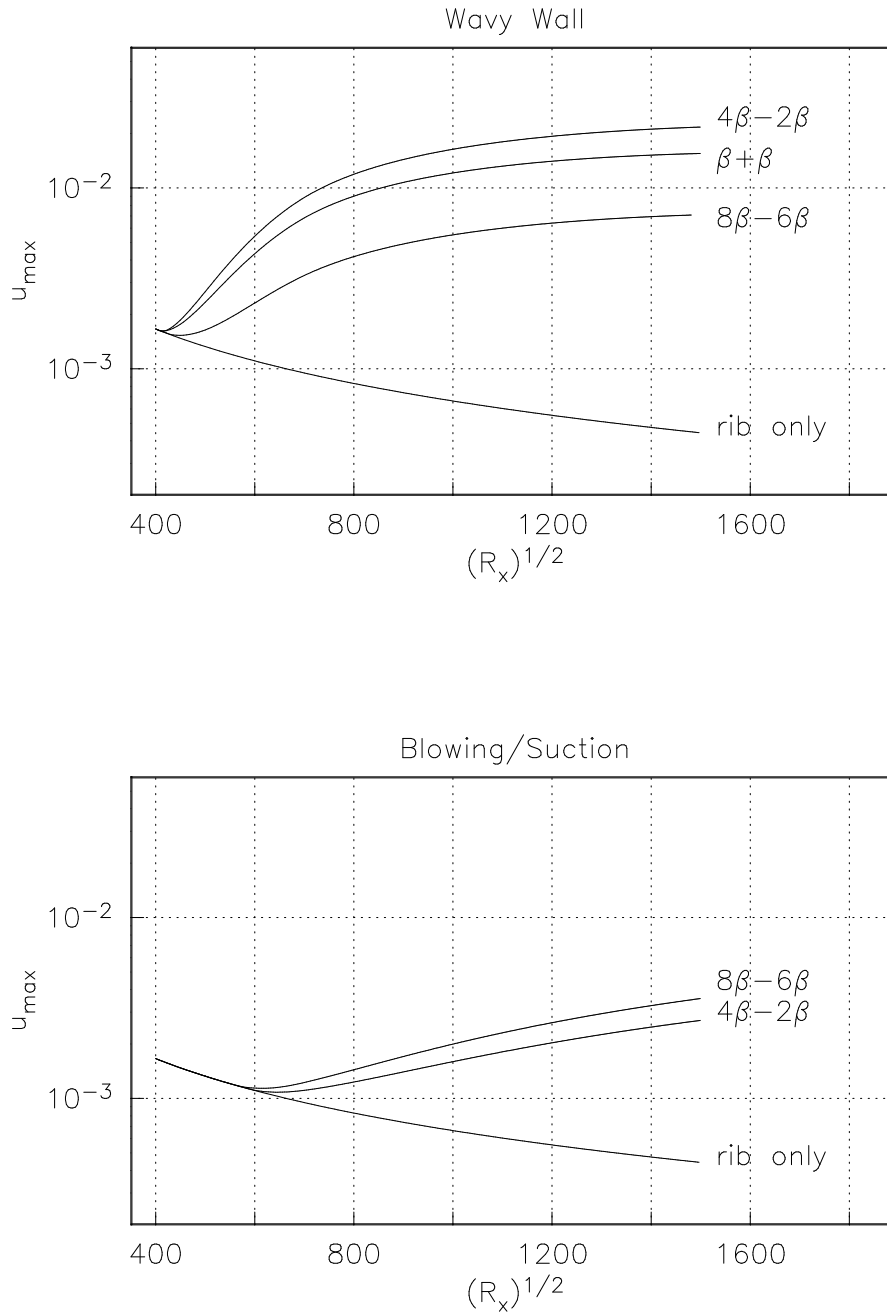


Figure 7: u_{max} amplitude versus Reynolds number of a vortex with spanwise wavenumber 2β flowing over a surface with modes $(0, \alpha, n\beta)$, where $\alpha = 1.0$, and $\beta = 0.15$. Top, surface modes corresponds to surface undulation; bottom, surface mode corresponds to blowing/suction. The line labeled “rib only” shows the amplitude of the vortex flowing over the streamwise ribs only.

of the Klebanoff mode [8], in addition to the possibility of algebraic growth as investigated by Herbert and Lin [9].

Figure 8b shows the velocity profiles of the vortex for the case $n = 1, m = 1$ of figure 8a. The u profiles agrees in shape with the experimental measurements of Kendall [10] of the Klebanoff mode.

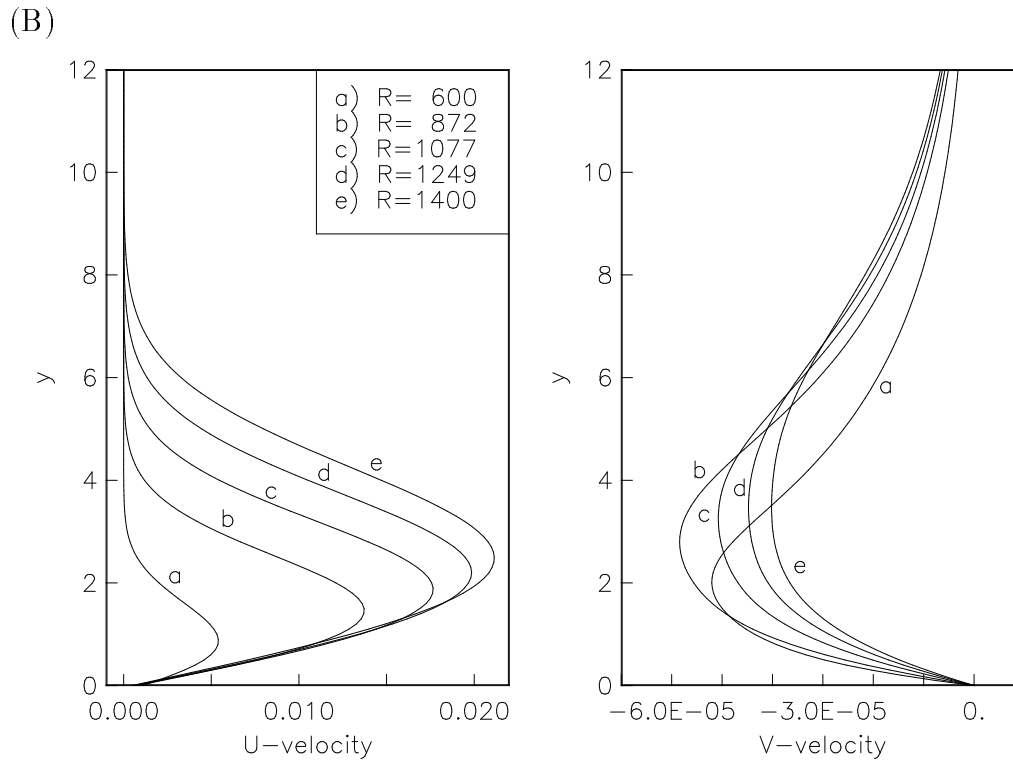
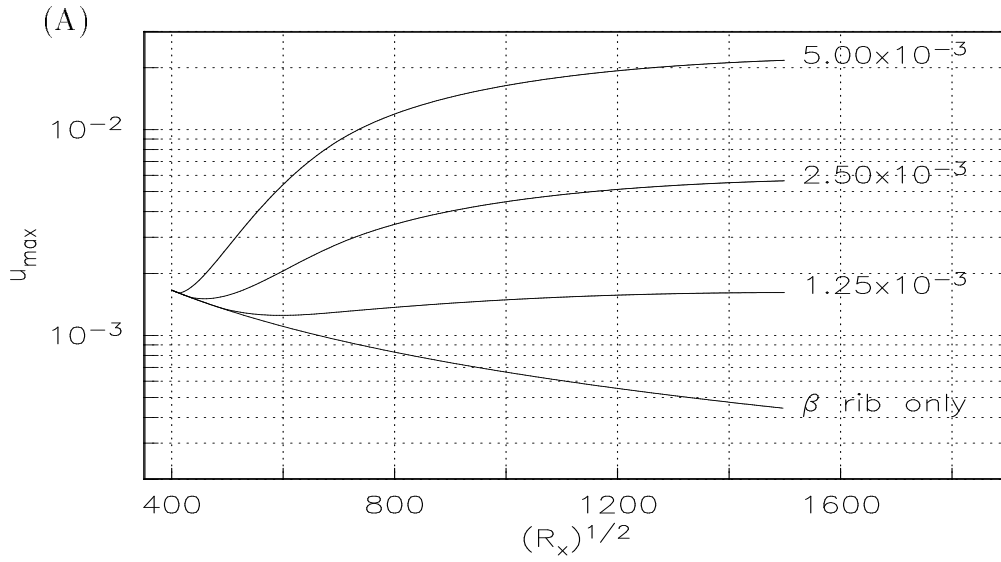


Figure 8: (a) Effect of surface height, $|\mathcal{W}|$, on the u_{\max} amplitude for a vortex with spanwise wavenumber 2β flowing over a surface with wavenumbers $(0, \alpha, 4\beta)$ and $(0, \alpha, 2\beta)$. (b) vortex u and v velocity profiles at various streamwise locations for the case $|\mathcal{W}| = 5 \times 10^{-3}$.

5 The effect of curvature on three-dimensional TS waves

We turn our attention now to three-dimensional TS waves and the effect that curvature has on them. The motivation for this study is two-fold. First, we look at the effect of curvature on disturbances that have a wave-vector orientation in between that of vortices (i.e. purely along z) and that of two-dimensional TS waves (i.e. purely along x). Second, the waves studied will be candidates for the nonlinear wave-vortex study, discussed in the next section.

In this study, the wall corrugations are omitted, leaving a smooth plate. The boundary conditions are homogeneous, leading to the classical eigenvalue problem for the TS waves. We solve for an augmented eigenvector composed of $\{u, v, \partial u/\partial x, \partial v/\partial x\}$ and an augmented eigenvalue $(a, da/dx)$ using the “local procedure” described in Bertolotti, Herbert & Spalart [11]. This procedure yields an improved solution over the standard Orr-Sommerfeld solution: in particular, it captures the increased effect of non-parallelism on three-dimensional waves (Bertolotti [12]). However, the procedure becomes invalid in the limit of low-frequency and long-wavelengths, where the governing equation cannot be reduced to ordinary differential form. In particular, the validity of the local procedure breaks down when the streamwise wavelength of the eigenmode becomes of order $\mathcal{O}(R)$, hence the procedure cannot reach the limit of pure vortices.

We use the local procedure because it allows the neutral curves to be traced efficiently in the R - F plane. Using the PSE solution, on the other hand, requires many runs at different frequencies in order to “raster-scan” the neutral curve, like, if you will, the electron beam on a TV screen.

The neutral stability curves, based on $\int_0^\infty u dy$, for TS waves having a fixed spanwise wavenumber, $\beta = 0.30$ and $\beta = 1.0$ are shown in figure 9. In the absence of curvature the low-frequency TS waves are stable, but with some curvature present a second region of instability appears near $F = 0$. Focusing on the $\beta = 0.3$ case, we see that as the curvature increases, two neutral curves form: the upper is the continuation of the curve for the flat plate; the second, at low frequencies, displays the fact that centrifugal instability is amplifying the Görtler vortices ($F = 0$) as well as modes with low frequency. At a curvature value of 8×10^{-4} the two curves merge. At this point there is a smooth connection between TS waves and the Görtler vortices.

The numbers along the outer neutral curve represent the wave-angle of the TS wave when $\mathcal{K} = 8 \times 10^{-4}$. The table below gives the phase-speed of the TS wave at the location where the symbol of the wave angle appears in figure 9. Note the increase in phase-speed as the frequency is lowered, and the wave-angle

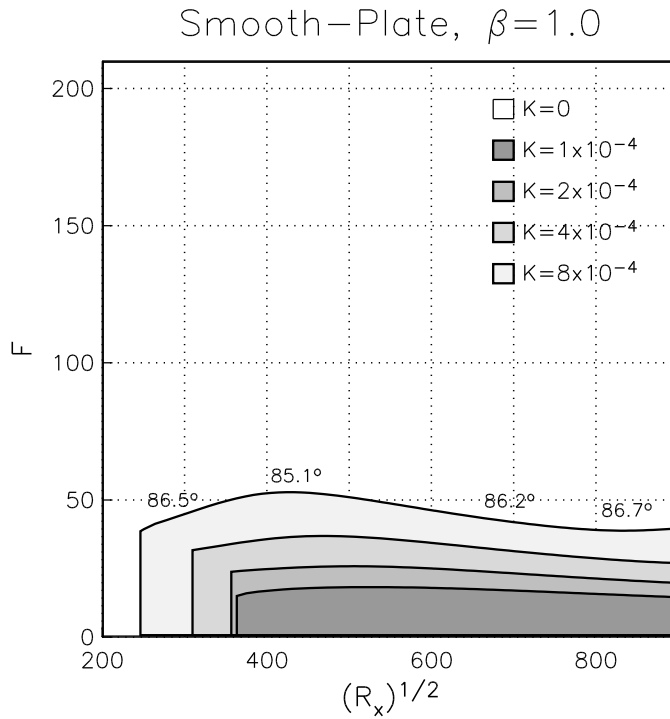
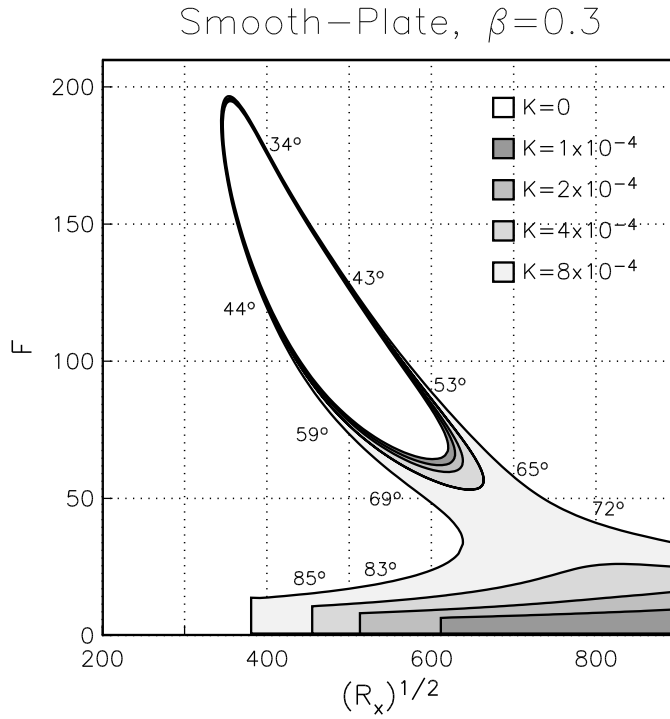


Figure 9: Effect of curvature, κ , on the neutral stability curves for 3-D Tollmien-Schlichting waves over a smooth plate. The numbers along the $\kappa = 8 \times 10^{-3}$ curve show the angle (deg.) of the wave-vector to the free-stream direction.

is increased.

Neutral curve, $\beta = 0.3$, $\kappa = 8 \times 10^{-4}$

Wave Angle (deg.)	Phase Speed
34.4°	0.4016
43.2°	0.3984
44.8°	0.3930
53.8°	0.4019
59.1°	0.4014
65.4°	0.4174
69.4°	0.4226
72.8°	0.4401
83.5°	0.5114
85.4°	0.5735

Neutral curve, $\beta = 1.0$, $\kappa = 8 \times 10^{-4}$

Wave Angle (deg.)	Phase Speed
85.1	0.6180
86.2	0.6510
86.5	0.6424
86.7	0.6829

TS waves with a $\beta = 1.0$ have a 1/3 shorter spanwise wavelength than those with $\beta = 0.3$, and, hence, are more densely packed. In the Blasius boundary layer, these waves are stable. Furthermore, the well-known types of nonlinear wave interactions, i.e. K-type and H-type, involve waves with β roughly equal to α , hence in the range $\beta < 0.5$. Thus, we must look at the growth rates to make some comments on importance of these densely packed waves.

Figure 10 compares the growth rates of a vortex with $\beta = 0.3$ and those of a TS wave with $\beta = 0.3$ and $F = 20$. The vortex grows over a fully corrugated wall, while the waves grow over a smooth wall. The growth rate of the vortex is greater than that of the TS wave, being roughly twice as large for the case of curvature $= \kappa = 8 \times 10^{-4}$. For comparison, the maximum growth rate of a 2-D TS wave with $F = 60$ is $\gamma = 0.0141$. Thus, the low-frequency 3-D TS wave undergo slower growth, but do so over a more extended streamwise distance.

We conclude this section with figure 11, which shows the variation of the receptivity coefficient in Crouch's receptivity model [1] with curvature for a 2-D TS wave at $F = 60$ and a 3-D TS wave with $F = 60$ and $\beta = 0.15$. The

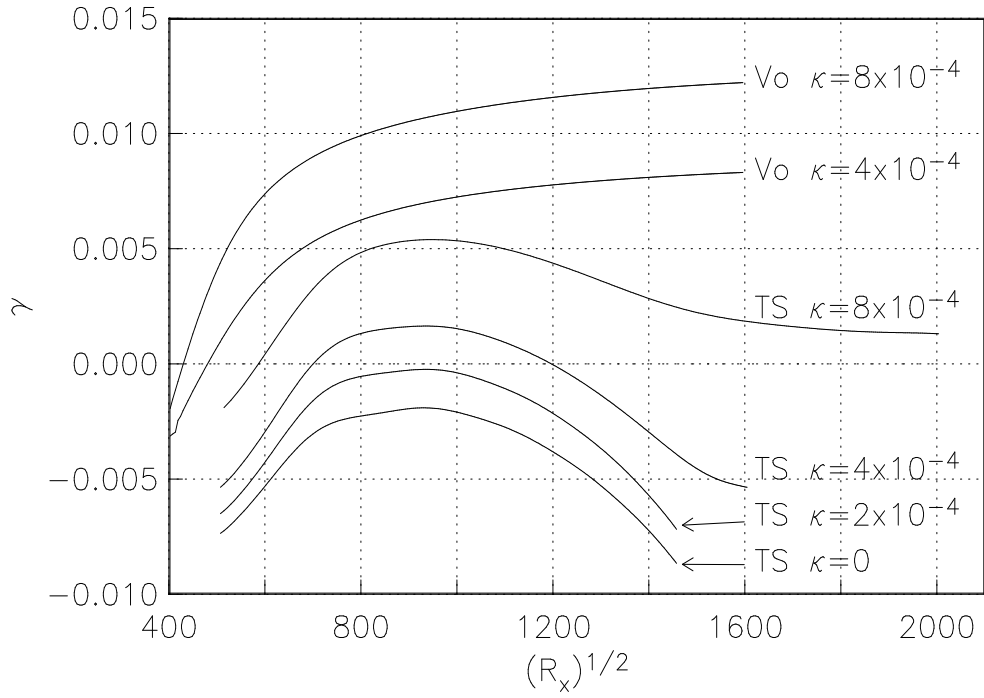


Figure 10: Comparison of growth rates, based on u_{max} , of a Görtler vortex with $\beta = 0.3$, and a TS wave of frequency $F = 20$ and $\beta = 0.3$, for various values of curvature.

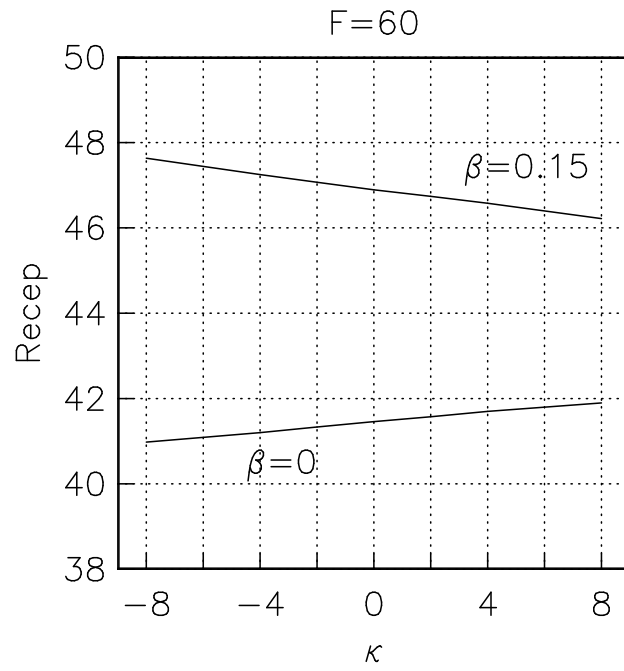
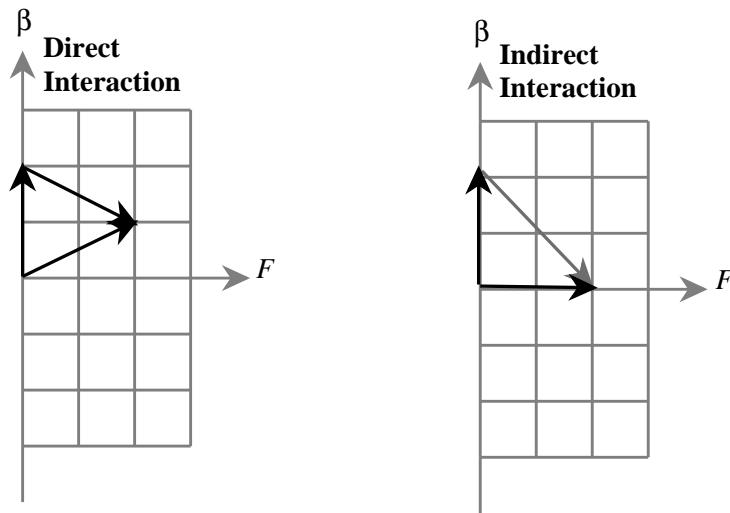


Figure 11: Effect of curvature on the receptivity coefficient for a two-dimensional TS wave, $\beta = 0$, and a three-dimensional TS wave, $\beta = 0.15$ with frequency $F = 60$.

data shows a weak influence of curvature on the receptivity mechanism (at this frequency).

6 Some case-studies of wave-vortex interaction.

The interaction between vortices and traveling waves in boundary-layers can play a major role in determining the transition location on swept wings. Partly for this reason, this interaction has been the focus of numerous studies.



The two possible ways a vortex and a wave can interact are shown in the figure above. The left diagram shows the triad interaction between a vortex and two oblique TS waves of equal frequency and streamwise wavenumber, but opposite spanwise wavenumber. We shall refer to this interaction as the “direct interaction”, since in a perturbation approach employing an expansion in amplitude, the waves interact at first order. The right diagram shows a triad interaction between a vortex, a two-dimensional traveling wave and a three-dimensional traveling wave. The traveling waves have equal frequency and a nearly equal streamwise wavenumber. The oblique vector is of a lighter shade of gray to indicate that its presence is not necessary at the onset of the interaction - this wave will be generated by the interaction between the vortex and the 2D wave, and will rise in amplitude to close the triad interaction. We shall refer to this interaction as the “indirect interaction”, since in a perturbation approach employing an expansion in amplitude, the waves interact, initially, at second order.

The direct interaction has been investigated more thoroughly than the indirect interaction. Studies of the direct interaction include those of Hall and Smith

[13] who employed a triple-deck asymptotic expansion in an analysis entitled “on strongly nonlinear vortex/wave interactions in boundary-layer transition”; Davis and Smith [14], who extended the investigation to three-dimensional boundary layers; Thumm, Wolz and Fasel [15], who looked at the interaction in a compressible boundary-layer using a direct numerical simulation, starting with only the oblique waves; Chang and Malik [16], who looked at the same case using the PSE equations; and Spalart [4], who employed a direct numerical simulation to look at the generation of cross-flow vortices by suction non-uniformities, and the subsequent breakdown induced by interaction with a TS wave.

With the exception of Spalart [4], the vortex in these investigations was generated by the nonlinear interaction of two oblique TS waves. Through this process, the vortex’s motion is “in tune” with the forcing provided by the traveling waves, and the triad interaction is optimal from a phase point of view. In our investigation the vortex and the traveling waves exist independently at the initial marching location, and may not be as much “in tune”. This difference may explain the lack of resonance found in the results presented below.

The indirect interaction was studied by Bertolotti [12]. The PSE equations were employed in a parametric study of the effect of initial amplitude levels and vortex spanwise wave-number on the location of “transition”, (defined as the onset of rapid spectrum filling). It was shown that vortex and TS wave behaved linearly up to the streamwise location where the oblique wave matched amplitudes with the vortex. Downstream of this location a strong resonance ensued, wherein the growth rates of the vortex and of the oblique wave were equal to one another, and were one order of magnitude larger than those given by linear calculations. These growth rates matched those given by Floquet theory for K-type transition. Figure 12, taken from Bertolotti [12], displays these results. The initial conditions consists of the (2,0) TS mode, and the (0,1) vortex. (In this work the disturbances were phased-locked, thus the index (2,0) stands for (2,2,0) in the current terminology). The dots represent the amplitude of the K-type secondary-instability wave with equal parameters β , F , and A_{TS} as in the vortex case. The agreement in slope between the dots and growth-rates of the vortex and the (2,1) mode indicates that these two modes undergo resonance as in the Floquet model. This figure was not published because the investigators felt that the way in which the vortex was initialized, namely by taking the limit of $F \rightarrow 0$ holding β constant in the local procedure was too arbitrary a choice.

In our study of wave-vortex interaction, we will include the receptivity mechanism. In this way, the initial conditions are specified by a small set of data, namely the description of the wall geometry and of the acoustic field present

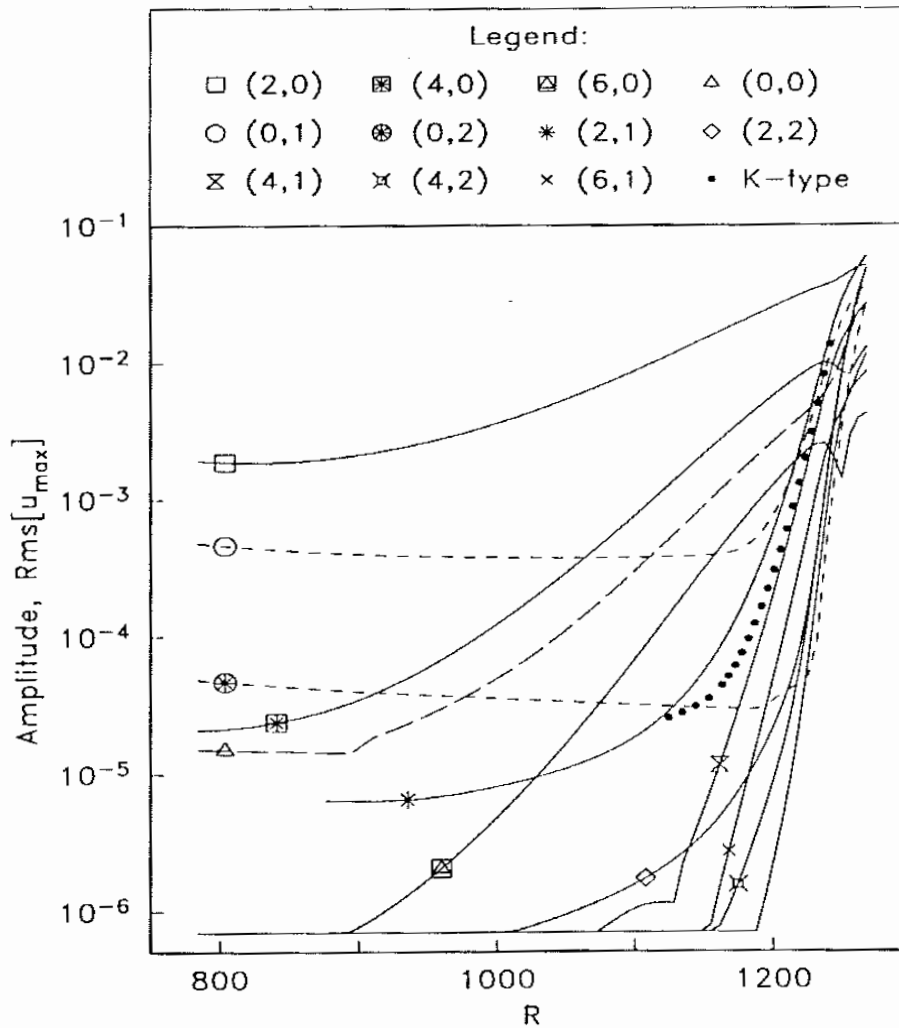


Figure 12: Wave-vortex indirect interaction: Amplitudes of selected modes versus Reynolds number. Initial conditions specified for the vortex and the (2,0) TS wave at frequency $F = 30$. The dots show the results from K-type secondary instability given by Floquet theory. (Plot taken from Bertolotti's PhD Thesis, page 165)

in the free-stream. We employ Crouch’s model [1] for the generation of the TS waves from the interaction of the acoustic field and the wall geometry. (See Bertolotti and Crouch [17] for details on the PSE implementation.)

Two TS frequencies were investigated, one at $F = 60$, representing the higher frequency modes, the other at $F = 20$, representing the lower frequencies. As shown in figure 9, low-frequency TS waves are amplified when concave curvature is present, and, thus, might play an important role in the transition process over concave surfaces. The curvature is held fixed at $\kappa = 2 \times 10^{-4}$. This small value of curvature is chosen because it leads to Görtler vortices with growth rates similar to those of the TS waves. If the curvature is increased to higher values, say 8×10^{-4} , then the growth of the vortex is too rapid to allow for significant interaction with the traveling waves, and at large amplitudes the vortex generates the transitional state suggested and investigated by Hall and Horseman [18], wherein the inflectional mean-flow profile induced by the vortex gives rise to inviscid (i.e. Rayleigh) instabilities.

At each frequency, two selections of surface roughness are used, a lower one with peak-to-peak variations in the range of $1 \times 10^{-3}\delta_o$, and a higher one with variations in the range of $1 \times 10^{-2}\delta_o$.

The parameters describing each case are listed in the table below:

Direct Interaction

	F=20		F=60	
	$\alpha = 0.0260, \beta = 0.15$		$\alpha = 0.0840, \beta = 0.15$	
	Low	High	Low	High
$\mathcal{W}_{(0,2,1)}$	1.0×10^{-3}	0.5×10^{-2}	0.5×10^{-3}	0.5×10^{-2}
$\mathcal{W}_{(0,0,2)}$	1.0×10^{-3}	1.0×10^{-3}	1.0×10^{-3}	1.0×10^{-3}

Indirect Interaction

	F=20		F=60	
	$\alpha = 0.03525, \beta = 0.15$		$\alpha = 0.09086, \beta = 0.15$	
	Low	High	Low	High
$\mathcal{W}_{(0,2,0)}$	2.0×10^{-3}	1.0×10^{-2}	1.0×10^{-3}	1.0×10^{-2}
$\mathcal{W}_{(0,0,1)}$	1.0×10^{-3}	1.0×10^{-3}	1.0×10^{-3}	1.0×10^{-3}

Since the mean-flow is independent of z , symmetric disturbances in z are assumed. To obtain peak-to-peak values, one must multiply $\mathcal{W}_{(0,n,0)}$ and $\mathcal{W}_{(0,0,n)}$ by 2, and $\mathcal{W}_{(0,n,m)}$ by 4 to take into account the complex conjugate modes.

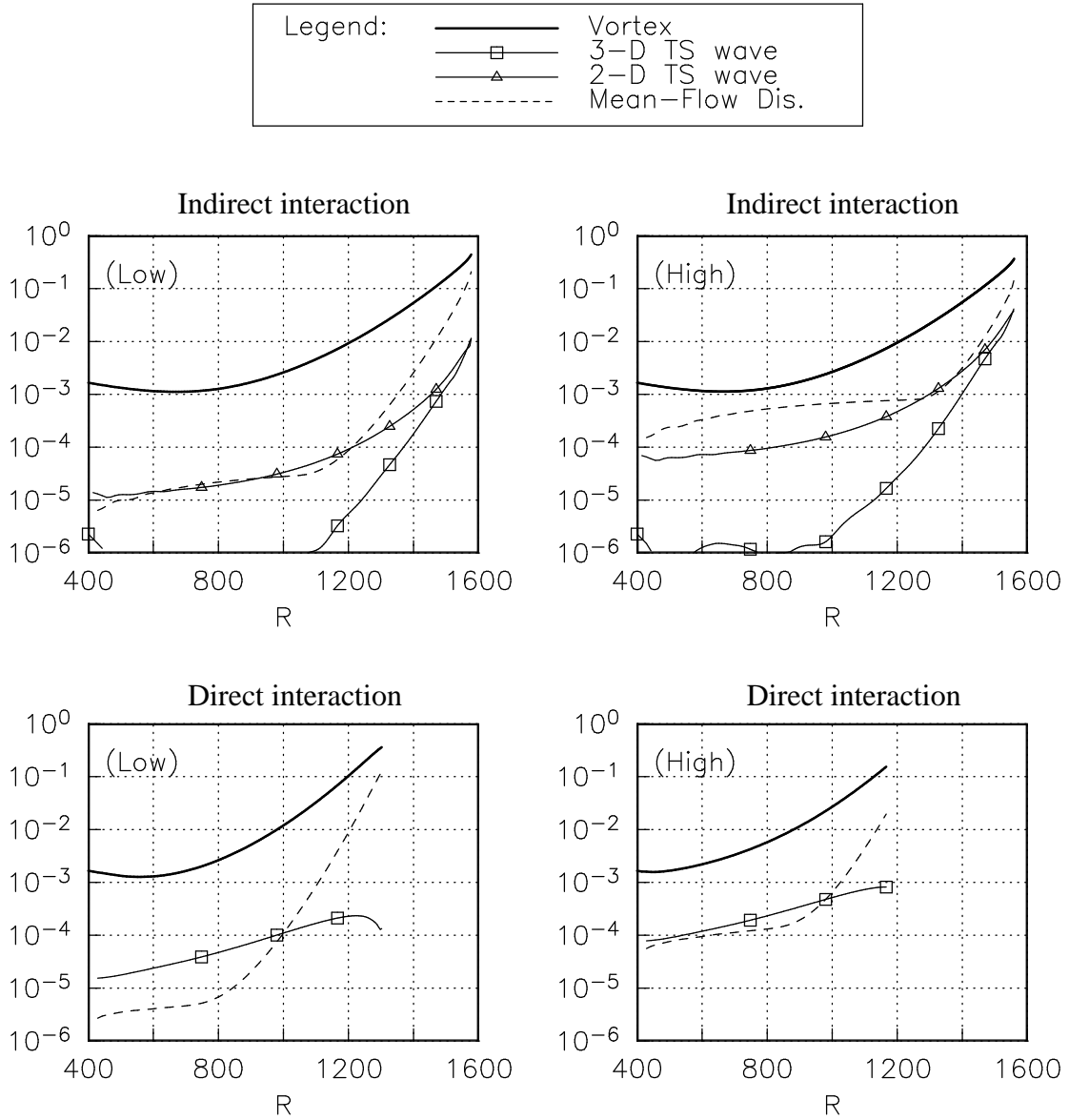


Figure 13: u_{max} amplitudes versus Reynolds number with a traveling-wave frequency of $F = 20$.

The amplitude evolution of the vortex, the traveling waves, and the mean-flow distortion are displayed in figure 13 for the frequency $F = 20$ and in figure 14 for the frequency $F = 60$. (These frequencies values refer to the traveling waves). Both the low and high wall roughness cases lead to a vortex-wave resonance in the case of the indirect interaction. The location of this resonance is only slightly affected by the level of the wall undulations.

On the other hand, the cases involving the direct interaction do not lead to a wave-vortex interaction. The traveling wave (i.e. mode (2,2,1)) is dampened past $R = 1200$, most likely due to the presence of the large mean-flow distortion induced by the vortex. The higher growth rate of the vortex in the “High” case is due to the receptivity of the vortex to the (2,2,1) wall mode, as discussed in section 5. The absence of a wave-vortex interaction is surprising, since the papers cited at the beginning of this section predict a strong resonance. A possible reason was thought to be due to an unfavorable phase relation between the vortex and the 3-D TS wave. However, changing the phase by 90 and 180 degrees did not change qualitatively the results. Thus, the reason for the lack of resonance remains at the moment unresolved.

The surface heights considered here are of the same order of magnitude as adhesive tape. The indirect interaction calculations, then, can help understand in a quantitative way Klebanov’s experiment [19], in which strips of adhesive tape were placed under the vibrating ribbon to help steady the transitional flow structure.

7 Conclusions

The response of vortices to surface inhomogeneities, both in the form of surface waviness and of wall-normal velocity, has been successfully investigated using the nonlinear PSE equations. Transients, and issues of algebraic growth, have been avoided through the use of a similarity solution as initial condition for the vortex.

In the absence of curvature, the vortex decays as $\sqrt{1/x}$ when flowing over streamwise aligned riblets of constant height, and grows as \sqrt{x} when flowing over a corresponding streamwise aligned variation of blowing/suction at the wall. However, in the presence of wall inhomogeneities having both streamwise and spanwise periodicity, the growth of the vortex can be much larger. In the presence of curvature, the vortex develops into a Görtler vortex.

The “direct” and “indirect” interaction mechanisms possible in wave-vortex interaction are presented. The “direct” interaction does not lead to strong resonance in the flow conditions investigated. The “indirect” interaction leads

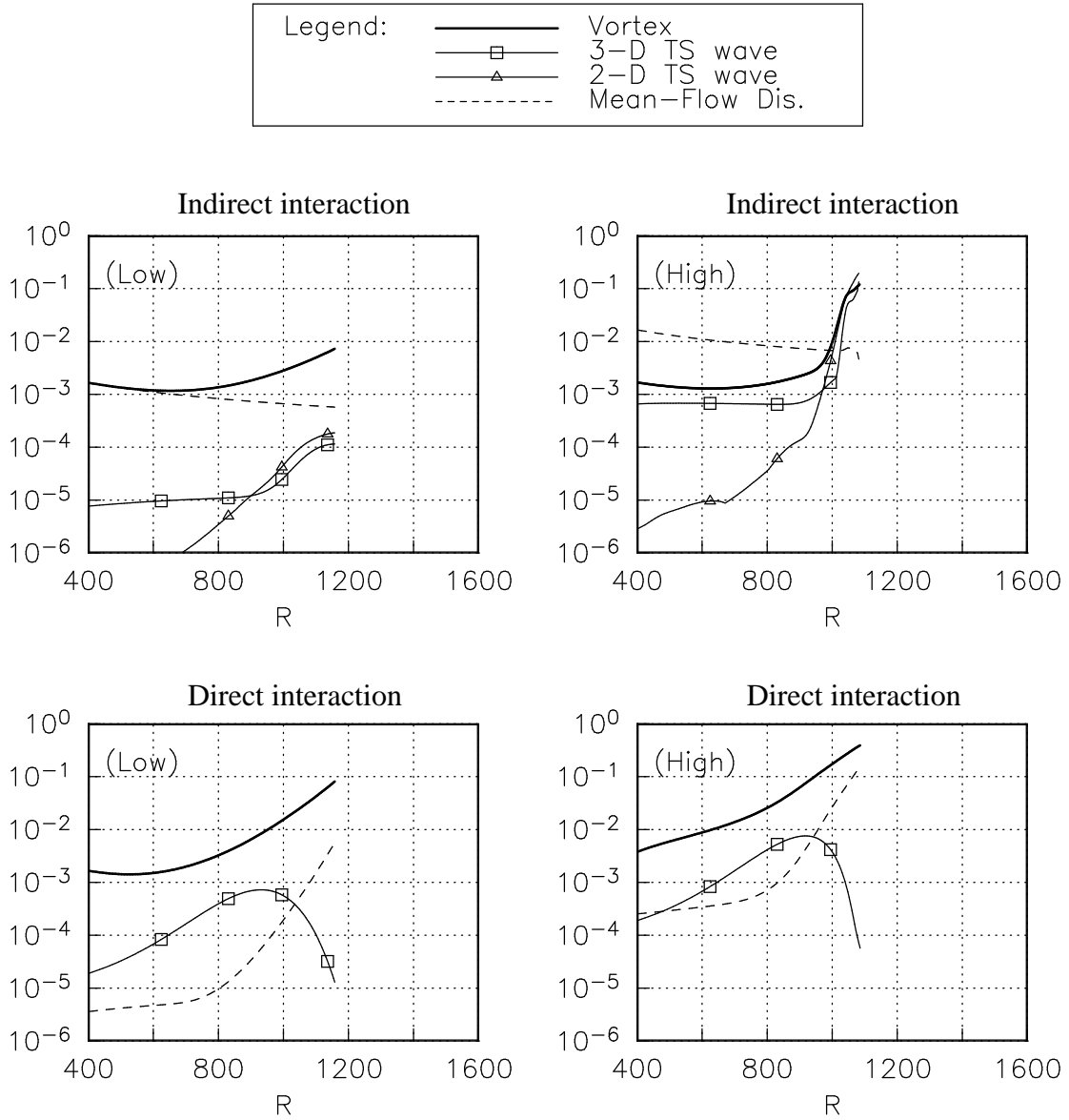


Figure 14: u_{max} amplitudes versus Reynolds number with a traveling-wave frequency of $F = 60$.

to K-type transition.

8 Acknowledgements

The helpful discussions with Dr. S. Otto on the nature of Görtler vortices, and their governing equations, are gratefully acknowledged. Dr. Jeff Crouch contributed helpful comments on the receptivity of traveling waves and vortices. This work was supported by NASA Contract No. NAS1-19480.

REFERENCES

1. J.D. Crouch, "Non-localized receptivity of boundary layers," *J. Fluid Mech.*, Vol. 224, pp. 567-581, (1992).
2. P.J. Schmid and D.S. Henningson, "A new mechanism for rapid transition involving a pair of oblique waves," *Phys. Fluids A*, to appear, (1992).
3. J. P. Denier, P. Hall and S. Seddougui, "On the receptivity problem for Görtler vortices: Vortex motions induced by wall roughness," ICASE Report 90-31, (1990). Submitted to *Journal Phil. Trans.*
4. P. S. Spalart, "Numerical studies of transition induced by suction devices," Near-Wall Turbulent Flows, R.M.C. So, C.G. Speziale and B. E. Launder (Editors), Elsevier Science Publishers B.V. (1993).
5. A. P. Bassom and P. Hall, "On the receptivity problem for $O(1)$ wavelength Görtler vortices," ICASE Report 93-58, (1993) (also as NASA Contractor Report 191519). Accepted to Proc. Roy. Soc. Lond. A.
6. J.D. Crouch and F.P. Bertolotti, "Nonlocalized receptivity of boundary layers to three-dimensional disturbances," AIAA Paper 92-0740 (1992).
7. J. Crouch, "Receptivity and the evolution of boundary-layer instabilities over short-scale waviness," *Phys. Fluids A*, Vol. 5 (3), pg. 561-567. (March 1993).
8. P. S. Klebanoff and K. D. Tidstrom, "Evolution of amplified waves leading to transition in a boundary-layer with zero pressure gradient," NASA TN D-195 (1959).
9. Th. Herbert and N. L. Lin, "Studies of boundary-layer receptivity with parabolized stability equations," AIAA Paper 93-3053 (1993).
10. J. M. Kendall, "Boundary-layer receptivity to freestream turbulence," AIAA Paper 90-1504.
11. F.P. Bertolotti, Th. Herbert and P.R. Spalart, "Linear and nonlinear stability of the Blasius boundary layer," *J. Fluid Mech.*, Vol. 242, pp. 441-474, (1992).
12. F.P. Bertolotti, *Linear and Nonlinear Stability of Boundary Layers with Streamwise Varying Properties*, PhD Thesis, The Ohio State University (1991).

13. P. Hall and F. T. Smith, "On the strongly nonlinear vortex/wave interactions in boundary-layer transition," *J Fluid Mech.*, Vol. 227, pg. 641-666 (1991)
14. D. A. R. Davis and F. T. Smith, "On the nonlinear Tollmien-Schlichting/Vortex interaction in three-dimensional boundary layers," NASA Technical Memorandum 106184, (1993).
15. A. Thumm, W. Wolz and H. Fasel, "Numerical simulation of spatially growing three-dimensional disturbance waves in compressible boundary-layers," Proceedings of the third IUTAM Symposium on Laminar-Turbulent Transition, Toulouse, France, Sept. 11-15 1989, (published 1990).
16. C.-L. Chang and M. R. Malik, "Oblique mode breakdown in a supersonic boundary layer using nonlinear PSE," Proc. First Euro. Comp. Fluid Dynam. Conference, Brussels, Belgium, Sept. 1992. Elsevier Science Publishers B.V.
17. F.P. Bertolotti and J.D. Crouch, "Simulation of boundary-layer transition: receptivity to spike stage," Proc. First Euro. Comp. Fluid Dynam. Conference, Brussels, Belgium, Sept. 1992, pp. 183-190. Elsevier Science Publishers B.V.
18. P. Hall and N. J. Horseman, "The inviscid secondary instability of fully nonlinear longitudinal vortex structures in growing boundary-layers," *J. Fluid Mech.*, Vol. 232, page 357, (1993).
19. P. S. Klebanoff, K. D. Tidstrom and L. M. Sargent, "The three-dimensional nature of boundary-layer instability," *J. Fluid Mech.*, Vol. 12, pg. 1-34. (1962).
20. Th. Herbert and F.P. Bertolotti, Bull. Am. Phys. Soc., **32** (1987) p. 2079.
21. Th. Herbert, "Boundary-layer transition analysis and prediction revisited," AIAA Paper 91-0737 (1991).
22. P. Hall, "The linear development of Görtler vortices in growing boundary layers," *J. Fluid Mech.*, Vol. 126, pg. 357. (1983).

9 Appendix A: The governing equations

We eliminate pressure by taking the curl of the Navier-Stokes equation. Since the flow field is harmonic in z , we can eliminate w using continuity, and then take the combinations of $\partial/\partial x(\mathbf{k}$ component) - $\partial/\partial z(\mathbf{i}$ component), and $\partial/\partial z(\mathbf{j}$ component) of the vorticity equation to obtain two equations governing u and v .

The resulting formulation offers two advantages over the original equations for the full set of primitive variables: reduced computational work, and PSE equations that are free from numerical instabilities at short marching steps.

We separate the flow field \mathbf{v}_T into the basic-flow, $\mathbf{V}_B(x, y)$ and the remainder $\mathbf{v}(x, y, z, t)$, which we call the disturbance. Our basic-flow is the Blasius boundary layer, and terms involving the second derivative with respect to x are of negligible magnitude. Excluding these terms, the governing equations for the disturbance components u and v are:

$$\begin{aligned}
& \left(\frac{\partial}{\partial t} + U_B \frac{\partial}{\partial x} + V_B \frac{\partial}{\partial y} - \frac{1}{R_o} \nabla^2 \right) \nabla^2 v + \frac{\partial Z_B}{\partial x} \left(2 \frac{\partial u}{\partial x} + \frac{\partial v}{\partial y} \right) + \\
& \frac{\partial Z_B}{\partial y} \frac{\partial v}{\partial x} + \frac{\partial^2 Z_B}{\partial x \partial y} v + \frac{\partial U_B}{\partial x} \left(\frac{\partial^2 v}{\partial x^2} - \frac{\partial^2 v}{\partial y^2} - \frac{\partial^2 v}{\partial z^2} - 2 \frac{\partial^2 u}{\partial x \partial y} \right) \\
& + \left\{ \frac{\partial^3 V_B}{\partial x \partial y^2} u + \frac{\partial V_B}{\partial x} \left(\frac{\partial^2 u}{\partial z^2} - \frac{\partial^2 u}{\partial y^2} \right) \right\} \\
& + 2\mathcal{K} \left[U_B \left(\frac{\partial^2 u}{\partial x^2} + \frac{\partial^2 u}{\partial z^2} + \frac{\partial^2 v}{\partial x \partial y} \right) + \frac{\partial U_B}{\partial x} \frac{\partial v}{\partial y} \right. \\
& \left. + \frac{\partial U_B}{\partial y} \frac{\partial v}{\partial x} + \left(2 \frac{\partial U_B}{\partial x} + \frac{\partial V_B}{\partial y} \right) \frac{\partial u}{\partial x} + V_B \frac{\partial^2 u}{\partial x \partial y} \right] = \\
& - \left(\xi \frac{\partial}{\partial x} + \eta \frac{\partial}{\partial y} + \zeta \frac{\partial}{\partial z} \right) \eta - \left(u \frac{\partial}{\partial x} + v \frac{\partial}{\partial y} + w \frac{\partial}{\partial z} \right) \left(\frac{\partial \zeta}{\partial x} - \frac{\partial \xi}{\partial z} \right) \\
& - \left(\frac{\partial \xi}{\partial z} \frac{\partial}{\partial x} + \frac{\partial \eta}{\partial z} \frac{\partial}{\partial y} + \frac{\partial \zeta}{\partial z} \frac{\partial}{\partial z} \right) u + \left(\frac{\partial \xi}{\partial x} \frac{\partial}{\partial x} + \frac{\partial \eta}{\partial x} \frac{\partial}{\partial y} + \frac{\partial \zeta}{\partial x} \frac{\partial}{\partial z} \right) w \\
& + \left(\frac{\partial u}{\partial z} \frac{\partial}{\partial x} + \frac{\partial v}{\partial z} \frac{\partial}{\partial y} + \frac{\partial w}{\partial z} \frac{\partial}{\partial z} \right) \xi - \left(\frac{\partial u}{\partial x} \frac{\partial}{\partial x} + \frac{\partial v}{\partial x} \frac{\partial}{\partial y} + \frac{\partial w}{\partial x} \frac{\partial}{\partial z} \right) \zeta \quad (4a)
\end{aligned}$$

$$\left(\frac{\partial}{\partial t} + U_B \frac{\partial}{\partial x} + V_B \frac{\partial}{\partial y} - \frac{1}{R_o} \nabla^2 \right) \left(\frac{\partial^2 u}{\partial x^2} + \frac{\partial^2 u}{\partial z^2} + \frac{\partial^2 v}{\partial x \partial y} \right)$$

$$\begin{aligned}
& -Z_B \frac{\partial^2 v}{\partial z^2} - \frac{\partial V_B}{\partial y} \left(\frac{\partial^2 u}{\partial x^2} + \frac{\partial^2 u}{\partial z^2} + \frac{\partial^2 v}{\partial x \partial y} \right) \\
& - 2\mathcal{K} \left[U_B \frac{\partial^2 v}{\partial z^2} + V_B \frac{\partial^2 u}{\partial z^2} \right] = \\
& \left(\xi \frac{\partial}{\partial x} + \eta \frac{\partial}{\partial y} + \zeta \frac{\partial}{\partial z} \right) \frac{\partial v}{\partial z} + \left(\frac{\partial \xi}{\partial z} \frac{\partial}{\partial x} + \frac{\partial \eta}{\partial z} \frac{\partial}{\partial y} + \frac{\partial \zeta}{\partial z} \frac{\partial}{\partial z} \right) v \\
& - \left(u \frac{\partial}{\partial x} + v \frac{\partial}{\partial y} + w \frac{\partial}{\partial z} \right) \frac{\partial \eta}{\partial z} - \left(\frac{\partial u}{\partial z} \frac{\partial}{\partial x} + \frac{\partial v}{\partial z} \frac{\partial}{\partial y} + \frac{\partial w}{\partial z} \frac{\partial}{\partial z} \right) \eta \tag{4b}
\end{aligned}$$

We have placed the nonlinear terms involving the product of disturbance quantities as right-hand-side terms because these terms will be lagged in the iterative process used to solve the system of equations.

The basic-flow terms on the third line of equation (4a) are negligible within boundary-layer theory. When the disturbance has velocity components of equal magnitude, such as a traveling wave, then these terms are negligible. However, when the disturbance has u and v velocity components that scale like those of the Blasius flow, such as vortices, then the terms on the third line of (4a) become of equal order to terms in the first two. Thus, in cases where the disturbance field includes both waves and vortices, as in the present study, these terms should be kept. In passing we note that, for steady vortices, equations (4a) and (4b) equal Hall's equations for Görtler vortices [22].

The parabolized stability equations, commonly abbreviated to PSE, were conceived by Herbert and developed by Herbert & Bertolotti [20] to incorporate nonlinearity and the slow growth of the boundary layer into the boundary-layer stability computations. The results were found to agree with those of full DNS simulations up to “spike stage”, where the complexity of the flow rapidly spreads beyond the resolution of the PSE code [11,12,21].

We express the disturbance velocity field in a series in time (index l), in x (index n) and in z (index k),

$$\mathbf{v}(x, y, z, t) = \sum_{l=-\infty}^{\infty} \sum_{n=-\infty}^{\infty} \sum_{k=-\infty}^{\infty} \mathbf{v}_{\mathbf{p}}(x, y, z, t) \tag{5}$$

where, \mathbf{p} is the wave-vector (l, n, k). The velocity field of each mode is partitioned into

$$\mathbf{v}_{\mathbf{p}}(x, y, z, t) = \hat{\mathbf{v}}_{\mathbf{p}}(x, y) \chi_{\mathbf{p}}(x, z, t). \tag{6}$$

The function

$$\hat{\mathbf{v}}_{\mathbf{p}}(x, y)$$

describes (in a sense made specific below) the velocity profile of each mode and the function χ incorporates the growth and wavelike part of the mode's velocity field

$$\chi_{\mathbf{p}}(x, z, t) = \exp \left[\int_{x_0}^x a_{\mathbf{p}}(s) ds + ik\beta z - il\omega t \right]. \quad (7)$$

where the complex wavenumber $a_{\mathbf{p}}$ is composed of a real growth rate, $\gamma_{\mathbf{p}}$, and an imaginary wavenumber $\alpha_{\mathbf{p}}$,

$$a_{\mathbf{p}} = \gamma_{\mathbf{p}} + i\alpha_{\mathbf{p}}$$

The partial differential equation governing the velocity profiles $\hat{\mathbf{v}}_{\mathbf{p}}$ is obtained by substituting the expansion (5) into equations (4a) and (4b). For the streamwise derivatives we make use of the slow change with x of the profiles and growth rates with the rule

$$\frac{\partial^m \mathbf{v}_{\mathbf{p}}}{\partial x^m} = \left[a_{\mathbf{p}}^m \hat{\mathbf{v}}_{\mathbf{p}} + m a_{\mathbf{p}}^{m-1} \frac{\partial \hat{\mathbf{v}}_{\mathbf{p}}}{\partial x} + \frac{m}{2} (m-1) a_{\mathbf{p}}^{m-2} \frac{da_{\mathbf{p}}}{dx} \hat{\mathbf{v}}_{\mathbf{p}} \right] \chi_{\mathbf{p}}, \quad (8)$$

where $a_{\mathbf{p}}(x) = \gamma_{\mathbf{p}}(x) + i\alpha_{\mathbf{p}}$. For $m > 1$ the streamwise derivatives of the mean-flow \mathbf{V}_B are zero, in accordance with the boundary-layer approximation. Similarly, in (8) we drop second- and higher-order derivatives with respect to x of $\hat{\mathbf{v}}_{\mathbf{p}}$ and $a_{\mathbf{p}}$. Performing harmonic balance yields an infinite set of coupled partial differential equations of parabolic type in x of the form

$$\mathbf{L} \hat{\mathbf{v}}_{\mathbf{p}} + \mathbf{M} \frac{\partial \hat{\mathbf{v}}_{\mathbf{p}}}{\partial x} + \frac{da_{\mathbf{p}}}{dx} \mathbf{N} \hat{\mathbf{v}}_{\mathbf{p}} = \sum_{\mathbf{r}} \mathbf{Q}[\mathbf{v}_{\mathbf{r}}, \mathbf{v}_{\mathbf{p}-\mathbf{r}}], \quad (9)$$

where the operators $\mathbf{L}, \mathbf{M}, \mathbf{N}$ and \mathbf{Q} contain derivatives with respect to y only. The summation on the r.h.s. of (9) is truncated to some number (L, N, K) in the numerical computations. Due to the symmetry in z we only need to solve for modes with non-negative wave numbers in t, x , and z . Upstream traveling modes are not allowed.

An ‘‘auxiliary’’ condition is needed in all PSE formulations to remove the ambiguity in (8) caused by the dependence of both $\mathbf{v}_{\mathbf{p}}$ and $a_{\mathbf{p}}$ on x . This condition has also been called a ‘‘normalization’’ condition in PSE literature. In our particular case we employ the condition,

$$\int_0^\infty \hat{u}_{\mathbf{p}}^\dagger \frac{\partial \hat{u}_{\mathbf{p}}}{\partial x} dy = 0 \quad (10)$$

where \dagger denotes the complex conjugate. Equations (9) and (10) form a complete set for the unknowns $\mathbf{v}_{\mathbf{p}}$ and $a_{\mathbf{p}}$.

We transfer the zero-slip wall boundary condition to $y = 0$ via a Taylor series expansion about $y = 0$, and stop the expansion at terms linear in $|H|$ since this quantity is assumed small, although including higher orders in $|H|$ can be done in a straight forward fashion. Performing harmonic balance yields the boundary conditions satisfied by $\hat{\mathbf{v}}_{\mathbf{p}}$ for each \mathbf{p} ,

$$\hat{\mathbf{v}}_{\mathbf{p}}(x, 0) = \frac{-1}{A_{\mathbf{p}}(x)} \left[\mathcal{W}_{\mathbf{p}} \frac{\partial \mathbf{V}_B(x, 0)}{\partial y} + \sum_{\mathbf{r}} \mathcal{W}_{\mathbf{p}-\mathbf{r}} \frac{\partial \hat{\mathbf{v}}_{\mathbf{r}}(x, 0)}{\partial y} A_{\mathbf{r}}(x) \right]. \quad (11)$$

where

$$A_{\mathbf{p}} = \exp\left[\int_{x_o}^x a_{\mathbf{p}}(s) ds\right].$$

The *xPSE* transition analysis tool-kit has been employed for the computations. The partial differential equations (9) are transformed into algebraic form by use of a multi-domain spectral collocation technique in y , and a finite difference discretization in x . Five domains are used in y , with limits at $[0, 1.6]$, $[1.6, 4]$, $[4, 14]$, $[14, 56]$, $[56, 96]$ (recall the reference length is δ^* at $R = 1000$), and u and v are approximated by 17 and 19 Chebychev polynomials, respectively, in each domain. Asymptotic boundary conditions are imposed at $y = 96$. For each mode \mathbf{p} , we construct the vector of unknowns

$$\mathbf{x}_{\mathbf{p}} = \{u_n, v_n, a\}_{\mathbf{p}}$$

composed of the Chebychev coefficients for u and v , and the complex wavenumber a for the mode, at the new marching location. The nonlinear algebraic system is solved iteratively by lagging the nonlinear terms one iterate, and using a Newton method to solve the linear problem

$$\nabla_{\mathbf{x}} \mathbf{F} \cdot \Delta \mathbf{x}_{\mathbf{p}} = -\mathbf{F}(\mathbf{x}_{\mathbf{p}}) + \mathbf{NL}_{\mathbf{p}} \quad (12)$$

for each mode \mathbf{p} . Here, the term $\mathbf{NL}_{\mathbf{p}}$ represents the nonlinear terms, and the function \mathbf{F} the terms in (4a) and (4b) that are linear in u and v .

10 Appendix B. The self-similar vortex

We approximate the vortex flow from the leading edge to the downstream location at which we begin the PSE simulations, say x_0 , with a self-similar form. Such a form satisfies continuity and the boundary conditions exactly, but produces a small residual error in the momentum equations. All terms of the Navier-Stokes equations reduce to terms dependent on the self-similar variable η except some coefficients, coming from z derivatives, that depend on x but with a variation sufficiently slow to allow the term to be approximated as constant. The curvature is set to zero.

The case of constant (in x) riblet height and the case of height proportional to \sqrt{x} , as well as the case of blowing/suction of constant (in x) strength and of decaying strength proportional to $\sqrt{1/x}$, yield quasi self-similar solutions. Herein we will focus on the constant amplitude cases. The surface geometry in the case of constant riblet height is described by the function,

$$H(x, z) = \mathcal{W}_{(0,1)} \exp[i\beta z] + c.c.,$$

where $\mathcal{W}_{(0,1)}$ is a real quantity that controls the height of the riblets. In the case of blowing/suction the wall velocity is given by the function,

$$V(x, z) = \mathcal{S}_{(0,1)} \exp[i\beta z] + c.c..$$

where $\mathcal{S}_{(0,1)}$ is a real quantity that controls the strength of the suction.

For the ribbed geometry we seek steady solutions of the form,

$$u(x, y, z) = u_{self}(\eta) e^{i\beta z} \sqrt{\frac{x_0}{x}} + c.c. \quad (13)$$

$$v(x, y, z) = v_{self}(\eta) e^{i\beta z} \frac{1}{x} + c.c. \quad (14)$$

$$w(x, y, z) = w_{self}(\eta) e^{i\beta z} \frac{1}{x} \sqrt{\frac{x_0}{x}} + c.c. \quad (15)$$

where $\eta = y\sqrt{x/x_0}$ is the Blasius similarity variable. For the suction case we seek steady solutions of the form,

$$u(x, y, z) = u_{self}(\eta) e^{i\beta z} \sqrt{xx_0} + c.c. \quad (16)$$

$$v(x, y, z) = v_{self}(\eta) e^{i\beta z} + c.c. \quad (17)$$

$$w(x, y, z) = w_{self}(\eta) e^{i\beta z} \sqrt{\frac{x_0}{x}} + c.c. \quad (18)$$

Reference length is x_0 !

Equation (1a) and equation (1b) become ordinary differential equations with independent variable η . These equations are, respectively,

$$\begin{aligned} a_0 u_{self} + a_1 u'_{self} + a_2 u''_{self} + \\ b_0 v_{self} + b_1 v'_{self} + b_2 v''_{self} + b_3 v'''_{self} + b_4 v^{iv}_{self} = 0 \end{aligned} \quad (19)$$

$$c_0 u_{self} + c_1 u'_{self} + c_2 u''_{self} + d_0 v_{self} = 0 \quad (20)$$

where the primes denote differentiation with respect to η . The formulation (?) for the constant riblet height yields,

$\begin{aligned} a_0 &= [5f'' + 7\eta f''' + \eta^2 f^{iv} + \mathcal{C}(f - \eta f' - \eta^2 f'')]/4 \\ a_1 &= \eta(3f'' + \eta f''')/2 \\ a_2 &= [\eta^2 f'' - \eta f' + f]/4 \\ b_0 &= -\eta f^{iv}/2 - 2f''' + \mathcal{C}(\mathcal{C} - f' + \eta f''/2) \\ b_1 &= -\eta f''' - f''/2 - \mathcal{C}f/2 \\ b_2 &= 2f' - \eta f''/2 - 2\mathcal{C} \\ b_3 &= f/2 \\ b_4 &= 1 \end{aligned}$	$\begin{aligned} c_0 &= \eta f''/2 + f'/2 - \mathcal{C} \\ c_1 &= f/2 \\ c_2 &= 1 \\ d_0 &= -f'' \end{aligned}$
--	---

while the formulation (?) for the constant suction yields,

$\begin{aligned} a_0 &= [f'' + 3\eta f''' + \eta^2 f^{iv} + \mathcal{C}(f - \eta f' - \eta^2 f'')]/4 \\ a_1 &= \eta(f'' + \eta f''')/2 \\ a_2 &= [\eta^2 f'' - \eta f' + f]/4 \\ b_0 &= -[\eta f^{iv} + f''' + \mathcal{C}\eta f'' + 2\mathcal{C}^2]/2 \\ b_1 &= -\eta f''' - f''/2 - \mathcal{C}f/2 \\ b_2 &= f' - \eta f''/2 - 2\mathcal{C} \\ b_3 &= f/2 \\ b_4 &= 1 \end{aligned}$	$\begin{aligned} c_0 &= \eta f''/2 - f'/2 \\ c_1 &= f/2 \\ c_2 &= 1 \\ d_0 &= -f'' \end{aligned}$
--	---

where $f(\eta)$ is the Blasius stream-function variable, and the symbol

$$\mathcal{C} = \beta^2 \frac{x}{x_0}$$

represents the coefficient that is dependent on x . The no-slip boundary conditions on the surface of the undulated wall are transferred to $y = 0$ via a Taylor

series expansion. These conditions are,

$$u_{self}(0) = -\mathcal{W}_{(0,1)} f''(0) \quad (21)$$

$$v_{self}(0) = 0 \quad (22)$$

$$v'_{self}(0) = 0 \quad (23)$$

while the boundary conditions for the suction case can be directly obtained,

$$u_{self}(0) = 0 \quad (24)$$

$$v_{self}(0) = \mathcal{W}_{(0,1)} \quad (25)$$

$$v'_{self}(0) = 0 \quad (26)$$

The condition on v'_{self} follows from continuity. The coefficient \mathcal{C} prevents the system of equations from being truly self-similar. As an approximation, we neglect the x/x_0 dependence in \mathcal{C} to arrive at a system of ordinary differential equations. This approximation is acceptable in view of the small values of β of interest - typically less than 0.1 (nondimensionalized with δ at the PSE starting location x_o). Thus, over the region $0 < x \leq x_o$, the magnitude of \mathcal{C} is less than $\beta^2 < 0.01$, which is small when compared to the order $\mathcal{O}(1)$ coefficients in (2a) and (2b).